

Iron Line Profiles in Strong Gravity

Kris Beckwith¹ and Chris Done¹

¹*Department of Physics, University of Durham, South Road, Durham DH1 3LE, UK*

Released 2004 Xxxxx XX

ABSTRACT

We describe a new code which can accurately calculate the relativistic effects which distort the emission from an accretion disc around a black hole. We compare our results for a disk which extends from the innermost stable orbit to $20r_g$ in both Schwarzschild and maximal ($a = 0.998$) Kerr spacetimes with the two line profile codes which are on general release in the XSPEC spectral fitting package. These models generally give a very good description of the relativistic smearing of the line for this range of radii. However, these models have some limitations. In particular we show that the assumed form of the *angular* emissivity law (limb darkening or brightening) can make significant changes to the derived line profile where lightbending is important. This is *always* the case for extreme Kerr spacetimes or high inclination systems, where the observed line is produced from a very large range of different emitted angles. In these situations the assumed angular emissivity can affect the derived *radial* emissivity. The line profile is not simply determined by the well defined (but numerically difficult) physical effects of strong gravity, but is also dependent on the poorly known astrophysics of the disc emission.

Key words: accretion discs - lines: profile -relativity

1 INTRODUCTION

Material in an accretion disk around a black hole is orbiting at high velocity, close to the speed of light, in a strong gravitational potential. Hence its emission is distorted by doppler shifts, length contraction, time dilation, gravitational redshift and lightbending. The combined impact of these special and general relativistic effects was first calculated in the now seminal paper of Cunningham (1975), where he used a *transfer function* to describe the relativistic effects. The observed spectrum from an accretion disc around a Kerr black hole is the convolution of this with the intrinsic disc continuum emission.

While such models have been used to try to determine the gravitational potential from the observed accretion disk spectra (e.g. Laor & Netzer 1989; Ebisawa, Mitsuda & Hanawa 1991; Ebisawa et al. 1993; Makishima et al. 2000; Gierlinski, Maciolek-Niedzwiecki & Ebisawa 2001), these attempts suffer from our limited knowledge of the spectral shape of the intrinsic accretion disk emission (see e.g. the review by Blaes 2002). It is much easier to determine the relativistic effects from a *sharp* spectral feature, such as the iron fluorescence line expected from X-ray illumination of an accretion disc (Fabian et al. 1989). An originally narrow atomic transition is transformed into broad, skewed profile whose shape is given *directly* by the transfer function.

Observationally, evidence for a relativistically smeared iron line first came from the ASCA observation of the active galactic nuclei (AGN) MCG-6-30-15 (Tanaka et al. 1995). Further observations showed evidence for the line profile being so broad as to require a maximally spinning black hole (Iwasawa et al. 1996). More recent data from XMM are interpreted as showing that the line is even wider than expected from an extreme Kerr disk, requiring direct extraction of the spin energy from the central black hole as well as the immense gravitational potential (Wilms et al. 2001).

Such results are incredibly exciting, but X-ray spectral fitting is not entirely unambiguous. There is a complex reflected continuum as well as the line (Nayakshin, Kazanas & Kallman 2000; Ballantyne, Ross & Fabian 2001). For an ionised disk (as inferred for MCG-6-30-15) the current models in general use (`pexrvt` in the XSPEC spectral fitting package) are probably highly incomplete (Ross, Fabian & Young 1999). Complex ionised absorption also affects AGN spectra (e.g. Kaspi et al. 2002) and the illuminating continuum itself can have complex curvature rather than being a simple power law.

However, in MCG-6-30-15 these issues have been examined in detail, and the results on the dramatic line width appear robust (Vaughan & Fabian 2003; Reynolds et al. 2004). Thus there is a clear requirement that the extreme relativistic effects are well modelled. There are two models which

are currently widely available to the observational community, within the **XSPEC** spectral fitting package, **diskline** (based on Fabian et al. 1989) and **laor** (Laor 1991). The analytic **diskline** code models the line profile from an accretion disc around a Schwarzschild black hole (so of course cannot be used to describe the effects in a Kerr geometry). Also, it does not include the effects of lightbending (although Fabian et al. 1989 outline a scheme for incorporating this) and hence does not accurately calculate all the relativistic effects for $r < 20r_g$ (where $r_g = GM/c^2$). By contrast, the **laor** model numerically calculates the line profile including lightbending for an extreme Kerr black hole, but uses a rather small set of tabulated transfer functions which limit its resolution and accuracy (see Section 3.3).

While there are other relativistic codes in the literature which do not suffer from these limitations, these are not generally readily and/or easily available for observers to use. There is a clear need for a fast, accurate, high resolution code which can be used to fit data from the next generation of satellites. In this paper we describe our new code for computing the relativistic iron line profile in both the Schwarzschild and Kerr metrics. We compare this with the **diskline** and **laor** models in **XSPEC** for discs which extend down to the last stable orbit in their respective spacetimes, and highlight both the strengths and limitations of these previous models.

2 CALCULATING STRONG GRAVITATIONAL EFFECTS

We follow the standard approach (e.g. Cunningham 1975; Fabian et al. 1989; Fanton et al. 1997) and calculate an infinitesimal amount of flux, dF_o observed at energy, E_o due to a patch on the disc which subtends a solid angle $d\Xi$ on the image of the disc at the observer (see Fig. 1 and 2).

$$dF_o(E_o) = I_o(E_o) d\Xi = g^3 I_e(E_e) d\Xi \quad (1)$$

where the redshift factor $g = E_o/E_e$ and specific intensity in the observers and emitters frame, I_o and I_e are related through the relativistic invariant I/ν^3 . For an emission line with rest energy E_{int} , then $I_e(E_e) = \varepsilon(r_e, \mu_e) \delta(E_e - E_{int})$, where $\varepsilon(r_e, \mu_e)$ is the emissivity, which can be a function of the radius, r_e and angle, μ_e at which the photon is emitted (as defined in Figure 1). The infinitesimal flux becomes

$$dF_o(E_o) = g^4 \varepsilon(r_e, \mu_e) \delta(E_o - gE_{int}) d\Xi \quad (2)$$

The total flux can be obtained by integrating over all the entire image of the disc in the observers sky. We can write $d\Xi = d\alpha d\beta / r_o^2$ where α, β are the x, y coordinates of the image of the disc at the observer with coordinates (r_o, θ_o) (see Figure 2), such that

$$F_o(E_o) = \frac{1}{r_o^2} \int \int g^4 \varepsilon(r_e, \mu_e) \delta(E_o - gE_{int}) d\alpha d\beta \quad (3)$$

The α, β position of the image of the disc section is related to the conserved quantities, λ, q which describe the contributions to the photons angular momentum from the radial, polar and azimuthal directions (de Felice & Preti 1999), via:

$$\alpha = -\frac{\lambda}{\sin \theta_o} \quad (4)$$

$$\beta = \pm \sqrt{q^2 - \lambda^2 \cot^2 \theta_o} \quad (5)$$

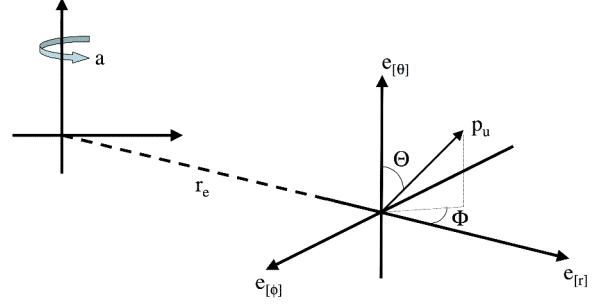


Figure 1. The coordinate system used for the disc. The emission is defined in the rest frame of the disc material. The polar and azimuthal emission angles Θ, Φ are obtained by taking the dot-products of the photon four-momentum with the basis vectors of this frame, where $\mu_e = \cos \Theta$. This disc frame can be connected to the frame which co-rotates with the black hole spacetime via a simple boost which depends on the velocity structure of the disc.

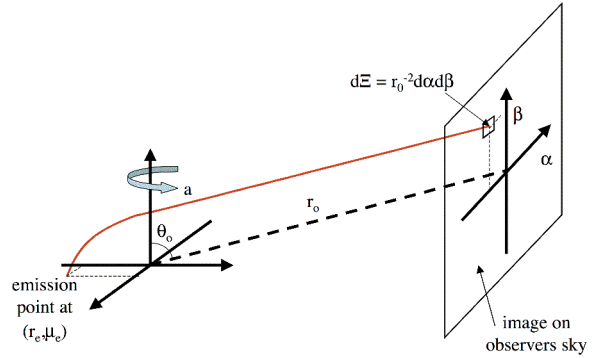


Figure 2. Diagram showing the link between the observers frame of reference and the global coordinate system defined by the black hole. Photons that are emitted from the disc at some distance r_e from the hole are seen at coordinates α, β on the image of the disc at the observer.

For a thin, Keplerian disc, these constants of motion can be written in terms of the redshift factor of the photon, g and the radius of emission, r_e and angle of emission, μ_e of the photon (as previously defined):

$$\lambda = \frac{1}{\Omega} \left(1 - \frac{e^{-\psi}}{g} \right) \quad (6)$$

$$q = \frac{r_e \mu_e}{g} \quad (7)$$

Here, Ω describes the azimuthal velocity profile of the emitting region and $e^{-\psi}$ is the 'redshift function' (Fanton et al. 1997; Martocchia 2000), which for a geometrically thin, Keplerian disc located in the equatorial plane are given by:

$$\Omega = \frac{1}{a + \sqrt{r_e^3}} \quad (8)$$

$$e^\psi = \left[1 - \frac{2}{r_e} (1 - a\Omega)^2 - (r_e^2 + a^2) \Omega^2 \right]^{-\frac{1}{2}} \quad (9)$$

Thus the problem reduces to finding the area on the observers sky subtended by all parts of the disc which contribute to a given E_o .

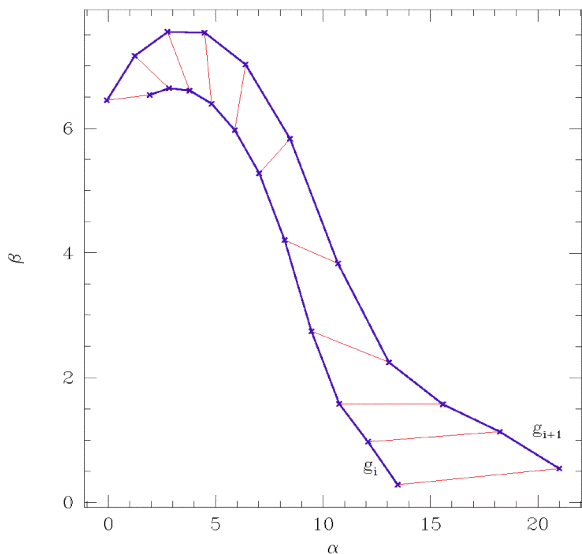


Figure 3. Heavy blue lines denote adjacent contours of constant redshift, $g_i < g_{i+1}$ on the observers sky (the α, β -plane) that define the area of the redshift bin $g = g_i + \frac{1}{2}(g_{i+1} - g_i)$ with width $dg = g_{i+1} - g_i$. Red narrow lines show examples of the divisions used to create a set of meshed trapezoids that enable the area of the redshift bin to be determined. For the purposes of clarity, this mesh is far coarser than that used in the calculations.

The photons (null geodesics) that link the accretion disc with the observer can only be found by determining the full general relativistic light travel paths which link the disc to the observer. These null geodesics are given by solutions of the geodesic equations (Carter 1968; Misner, Thorne and Wheeler 1973; Chandrasekhar 1983), which can be obtained numerically (e.g. Karas, Vokrouhlicky & Polnarev 1992), but can also be given in terms of analytic functions (Rauch & Blandford 1994; Agol 1997; Cadez, Fanton & Calvani 1998), which enable them to be solved quickly and with arbitrary accuracy.

We develop a technique based solely on the image of the accretion disc in the α, β plane, which defines the flux received by the observer, similar to that employed by Cadez, Calvani & Fanton (2003). This allows us to generate high resolution, accurate line profiles numerically while avoiding the issues surrounding the partial derivatives of the geodesic equations (Viergutz 1993). We use the analytic solutions of the geodesic equations as tabulated by Rauch & Blandford (1994) to find the complete set of light travel paths that link the accretion disk and the observer at (r_o, θ_o) . We sort these by redshift factor, and use adaptive gridding to find the boundaries on the (α, β) -plane for all lines of constant g .

Two adjacent boundaries, g_i and g_{i+1} , therefore define the area of the redshift bin $g = g_i + \frac{1}{2}(g_{i+1} - g_i)$ with width $dg = g_{i+1} - g_i$ when projected onto the (α, β) -plane (as is shown in Figure 3). We can simply determine the area of this region by dividing it up into a set of tessellating trapezoids, as shown in Figure 3, the area of each of which can be determined by a simple geometric formula. The final area of the redshift bin is determined by summing together the contributions from all such trapezoids internal to (g_i, g_{i+1}) .

Each individual trapezoid is small, so that there is no significant change in r_e or μ_e (though this is not necessarily true across the total area $d\alpha d\beta$). The emissivity law can be convolved into the calculation using the emission coordinates at the centre of each trapezoid to weight its area before performing the summation over all trapezoids. This approach allows us to calculate line profiles at high spectral resolution on timescales of a few minutes on a 2GHz desktop PC.

We have extensively tested the routines that calculate the null geodesic paths against those supplied by Eric Agol (Agol 1997) and have found them to be indistinguishable. We have also compared the line profiles generated by our code to those presented previously in the literature, in particular those generated from the code described by Fanton et al. (1997) and have again found them to be indistinguishable.

3 HIGHLY RELATIVISTIC LINE PROFILES

3.1 Introduction

We have taken a disc from r_{ms} to $r_{max} = 20r_g$ (beyond which strong gravitational effects become of diminishing importance) for both the Schwarzschild ($a = 0$, $r_{ms} = 6r_g$) and maximal Kerr ($a = 0.998$, $r_{ms} = 1.235r_g$) cases for $\theta_o = 5^\circ, 30^\circ, 60^\circ$ and 85° .

We first consider the extent of lightbending effects in a Schwarzschild spacetime. Figure 4 shows the three-dimensional surface in (μ_e, r_e, g) for the complete set of light travel paths connecting the accretion disc to the observer. There is a considerable range of μ_e contributing to the observed emission at all inclinations. For low inclinations the effect is fairly uniform, with each radius contributing a similar range in μ_e , but with a systematic shift to larger emission angles (smaller μ_e) with smaller radii. By contrast, at higher inclinations the lightbending is strong enough to gravitationally lens the far side of the disc. This leads to a much larger range of μ_e which contribute to the disc image at small radii. In all cases, lightbending means there *is* a range of μ_e which contribute to the observed disc emission, so that in general, the line profile *will* depend on the angular distribution of the emitted flux.

Fig. 5 shows the corresponding surfaces for the extreme Kerr case. The disc now extends down to $1.235r_g$, far closer to the corresponding event horizon than in the Schwarzschild case. This introduces a greater complexity to the geodesic surfaces. The range of emission angles is from zero to unity in all cases, including the nearly face on disc at 5° , which has important consequences for the calculation of the line profile.

To construct the relativistic line profile, we map these surfaces on to the (α, β) plane as discussed in the previous section, forming images of the accretion disc, as have been previously calculated by e.g. Cunningham & Bardeen (1973); Luminet (1979); Hollywood & Melia (1997); Fanton et al. (1997); Falcke, Melia, & Agol (2000). In Figure 6 we present images of the Schwarzschild disc for the 30° (top row) and $\theta_o = 85^\circ$ (bottom row) cases (others provide no new information qualitatively). Images on the left-hand side of the figure are coloured by values of the redshift factor, g , as defined by the scale at the top of each image.

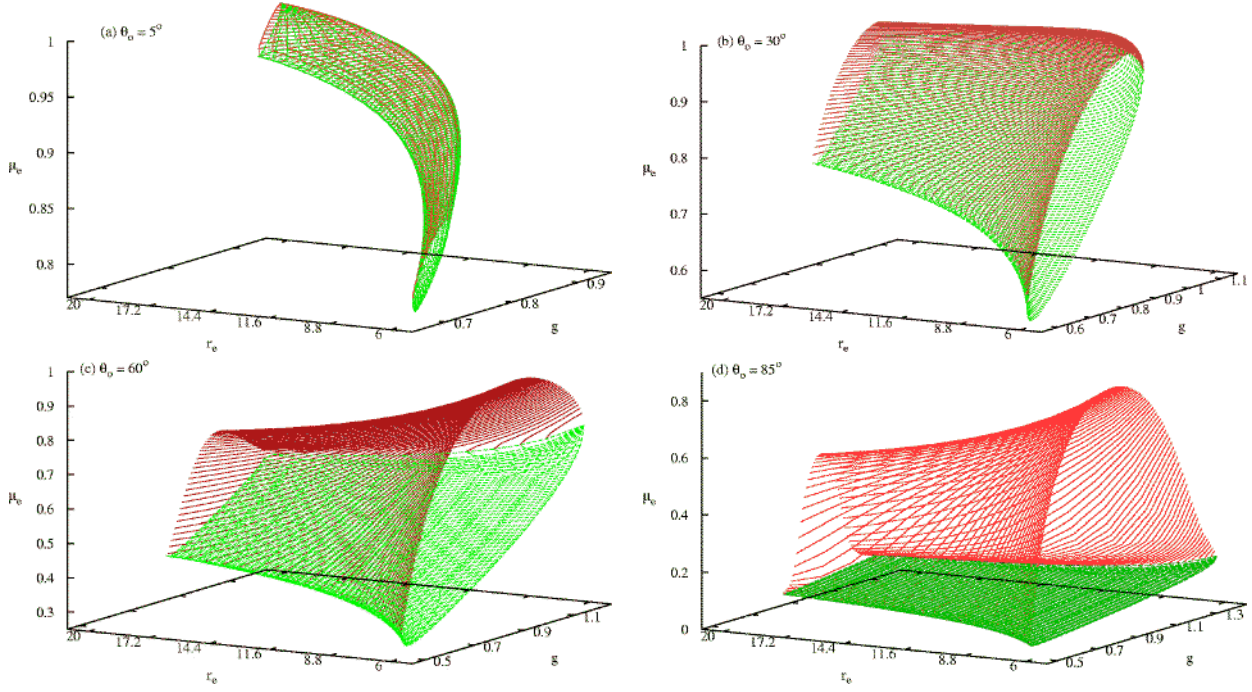


Figure 4. Surfaces in the (μ_e, r_e, g) parameter space describing geodesics that reach an observer at a given inclination for a standard accretion disk around a Schwarzschild black hole. Notice that, for every (r_e, g) pair, there are two geodesics that reach any given observer, corresponding respectively to geodesics that are emitted from the side of the disc closest to the observer (lower surface) and geodesics that are emitted from the opposite side of the disc to the observer (upper surface). These are the two geodesics referred to by Cunningham (1975).

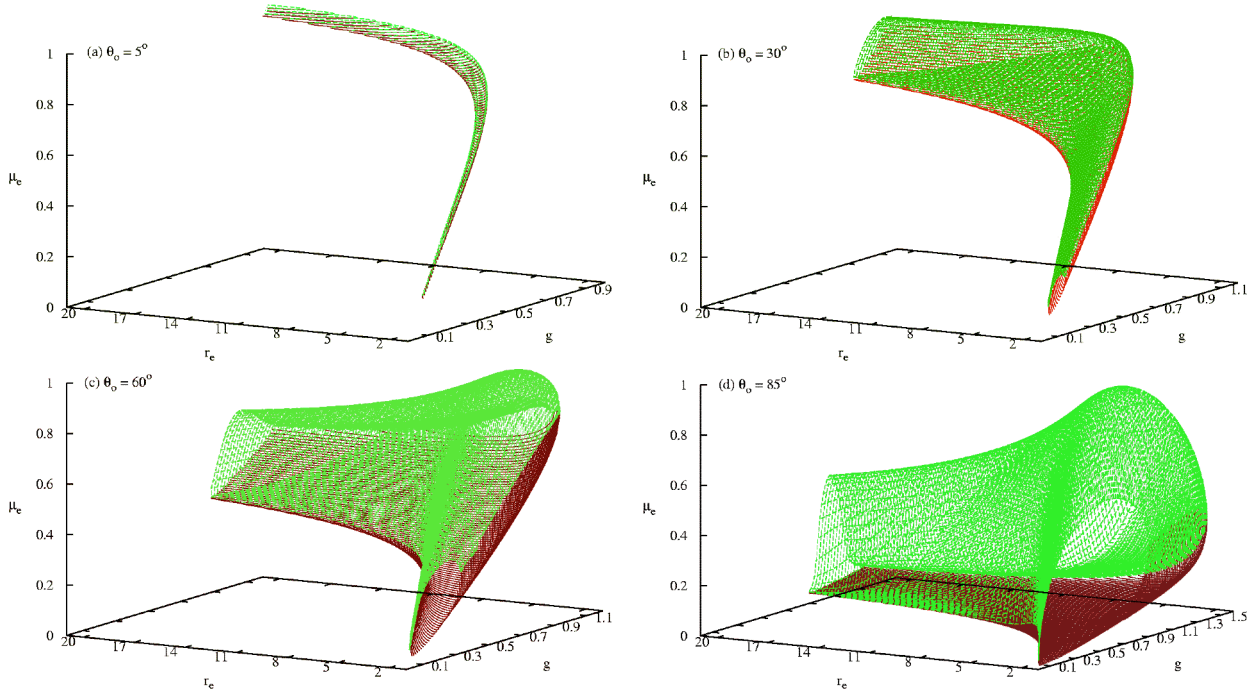


Figure 5. As in Figure 4 for a maximal ($a = 0.998$) Kerr black hole. These surfaces exhibit a far greater complexity than those in the Schwarzschild case. The range of accessible redshift is increased for a given disc-observer system, whilst the range of emission angles is from zero to unity for all inclinations.

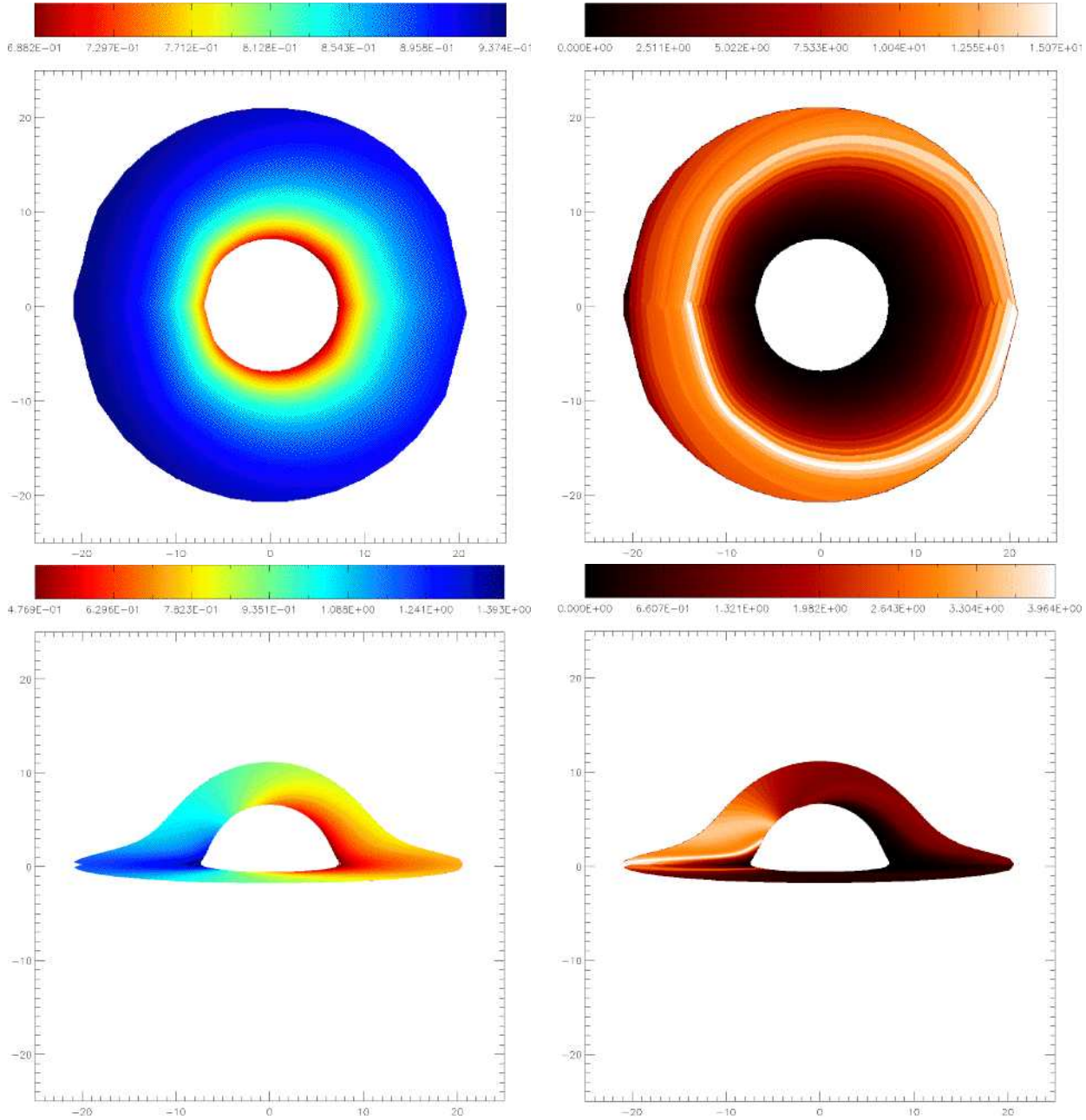


Figure 6. Redshift images (left hand panels) and flux image (right hand panels) of the accretion disc on the (α, β) plane for a Schwarzschild black hole, for the $\theta_o = 30^\circ$ (top row) and $\theta_o = 85^\circ$ (bottom row) cases. Redshift images are coloured by the associated values of g as measured by the distant observer. Flux images colored by the $g^4 r_o^2 d\Xi = g^4 dad\beta$ component of the relativistic line profile. Note the appearance of strong light bending effects in the $\theta_o = 85^\circ$ case, as previously reported by Matt, Perola and Stella (1993), Zakharov and Repin (2003).

By contrast, images on the right-hand side of the figure has each redshift bin coloured by its area on the observers sky, i.e. $g^4 dad\beta$, again with the scale defined at the top of each image. Strong gravitational lensing effects can now clearly be seen in the high inclination images. Photons from the far side of the disc pass close to the black hole, so the disc image is strongly distorted (Matt, Perola & Stella 1993; Zakharov & Repin 2003). Since the area of the disc is magnified, its contribution to the observed flux should be

large. However, we stress that the low inclination images *are* also affected by lightbending (see Figure 4a and 5a), though they are not magnified by gravitational lensing.

The form of the line profile is now determined from the flux image (representing the effects of strong gravity), together with the assumed form for the emissivity (determined by the energy release and radiative transfer processes), which is generally taken as (ignoring azimuthal de-

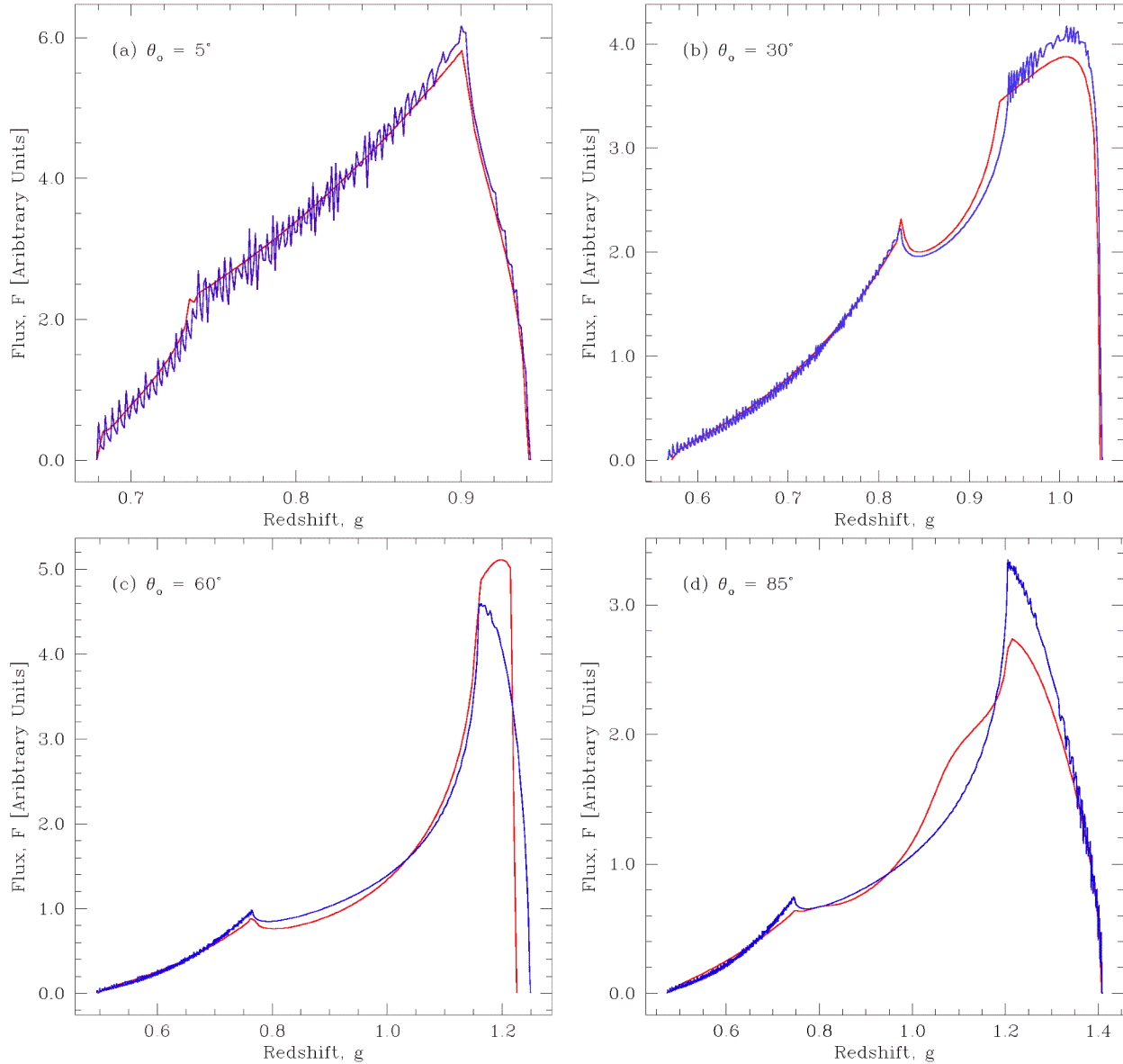


Figure 7. Comparison of the relativistic line profile computed by our model (red solid line) with that computed by the `XSPEC diskline` model (blue dashed line) for $\epsilon(r_e) \propto r^{-3}$ and $f(\mu_e) = 1$. At inclinations of $< 30^\circ$, the profiles match to within $\sim 10\%$, but the increasing importance of lightbending (which is not included in the `diskline` code) gives a 40% discrepancy in the profile shapes for inclinations $> 60^\circ$. In this and all subsequent figures the line profiles are normalised such that they contain one photon, and all our results are unsmoothed.

pendence):

$$\varepsilon(r_e, \mu_e) = \epsilon(r_e) f(\mu_e) \quad (10)$$

While the flux image is a difficult numerical problem, it depends on well known *physics*. By contrast, the emissivity laws considered have rather simple forms, but are determined by the poorly known *astrophysics* of the disc. Of course, there are many other outstanding theoretical issues that can produce a substantial impact on the line profile, including (but not limited to) returning radiation or lightbending that can enhance the emissivity of the inner part of the disc (Cunningham 1975; Laor, Netzer & Piran 1990; Martocchia, Karas & Matt 2000), emission from the plung-

ing region (Reynolds & Begelman 1997) and azimuthal dependence of the emissivity (Cadez, Calvani & Fanton 2003; Karas, Martocchia & Subr 2001). However, these are outside the scope of the current work.

3.2 Comparison with the Diskline Model

The `diskline` code assumes a Schwarzschild metric ($a = 0$) and additionally that light travels in straight lines (so the angular emissivity term is irrelevant). In its `XSPEC` implementation it allows both arbitrary power law $\epsilon(r_e) \propto r^q$ and point source illumination. However, its analytic structure means that any radial emissivity law is easy to incorpo-

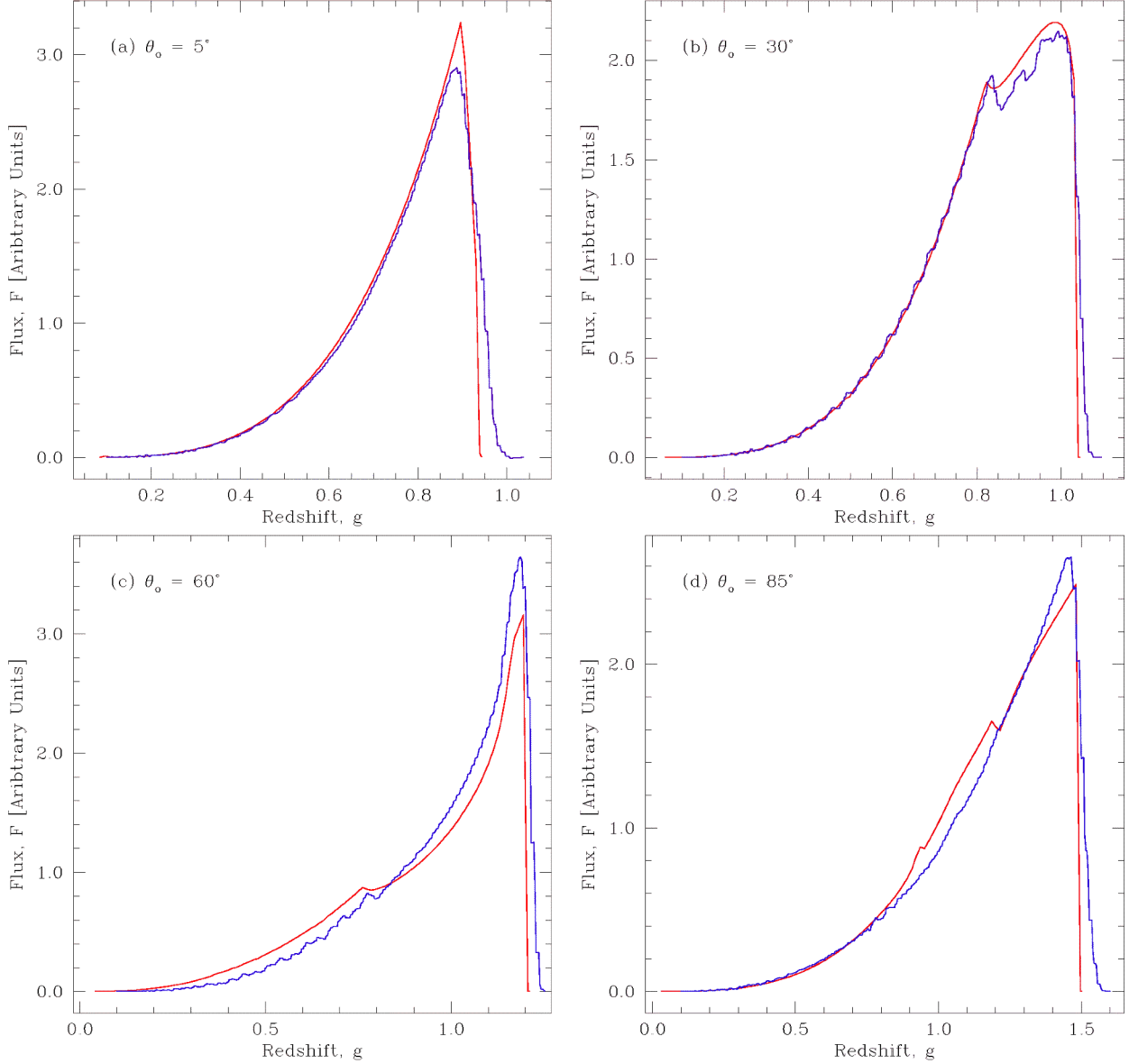


Figure 8. Comparison of the relativistic line profile computed by our model (red solid line) with that computed by the XSPEC `laor` model (blue dashed line) for $\epsilon(r_e) \propto r^{-3}$ and $f(\mu_e) \propto (1 + 2.06\mu_e)$. The profiles produced by the two models match to within 5 – 10%.

rate. We choose to use $q = -3$, as this is approximately the form of the gravitational energy release per unit disc area (see e.g. Zycki, Done & Smith 1989).

Figure 7 shows our line profiles assuming $f(\mu_e) = 1$ (no angular dependance of the emissivity) compared with those from the `diskline` code. We see that our new model matches very closely to the XSPEC `diskline` model for a nearly face on disk. Whilst the key difference between our model and `diskline` is the inclusion of light-bending effects, the impact of this is small at low inclinations if there is no angular dependance to the emissivity (but see Section 3.4).

By contrast, at high inclinations, lightbending not only means that the line is formed from many different μ_e , but gravitational lensing enhances the flux from the far side of the disc. This lensing effect gives clear differences between our model and `diskline`. The lensing magnifies the image of

the far side of the disc, which has velocity mostly tangential to the line of sight, so is not strongly doppler shifted. This boosts the line profile at $g \sim 1$ (see Matt, Perola & Stella 1993). Since the line profiles are all normalised to a single photon, then this also makes the blue peak smaller.

In summary, the `diskline` model as incorporated into XSPEC produces line profiles which are accurate to $\sim 10\%$ for inclinations of less than 30° . Obviously, if the inner disc edge $r_{min} > r_{ms}$ then the lightbending effects become correspondingly smaller and the match between the two codes becomes even closer. At higher inclinations the differences between `diskline` and our code become larger due to the effects of gravitational lensing, which leads to an effective redistribution in flux between the blue peak and the center of the line compared to that predicted from straight light travel paths.

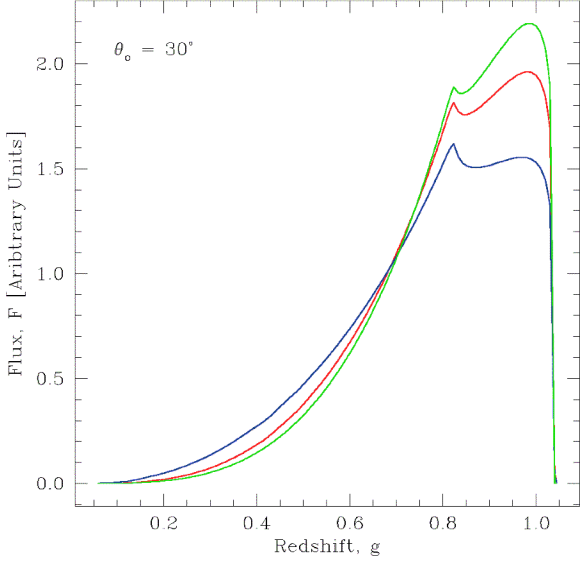


Figure 9. Comparison of the relativistic line profiles generated by our model with (a) $\epsilon(r_e) \propto r_e^{-3}$, $f(\mu_e) = 1$ (red lines), (b) $\epsilon(r_e) \propto r_e^{-3}$, $f(\mu_e) \propto \mu_e^{-1}$ (blue lines), (c) $\epsilon(r_e) \propto r_e^{-3}$, $f(\mu_e) \propto (1 + 2.06\mu_e)$ (green lines) for a maximal Kerr black hole with the disc extending from $1.235 - 20r_g$. The relative height of the blue wing changes by $\sim 35\%$ for different angular emissivity laws, anti-correlated with the slope of the red wing.

3.3 Comparison with the Laor Model

By contrast, the **laor** code is written for extreme Kerr, and includes a standard limb darkening law $f(\mu_e) \propto (1 + 2.06\mu_e)$. The code is based on a series of photon trajectory calculations, where the disc is split up into a set of rings of width dr_e at r_e . Each part of the ring radiates with total emissivity (radial plus angular) given simply by the limb darkening law (i.e. no radial dependence, $q = 0$) and the line profile from that ring is built up from many light travel paths which connect the disc to the observer. This produces a series of *transfer functions* $T(r_e, E_o - gE_{int})$ at each radius, analogous to Figure 6a–d but including the limb darkening law. These tabulated transfer functions are read by the **laor** code in XSPEC and used to build a total line profile for any given radial emissivity $F_o(E_o) = \int \epsilon(r_e)T(r_e, E_o - gE_{int})r_e dr_e dg$.

We compare this with our code, using a $q = -3$ emissivity for both as in the **diskline** comparisons above. We include the same limb darkening law as used by **laor** and the results (Figure 8) show that the overall match between our code and **laor** is good to $\sim 5 - 10\%$.

4 THE ROLE OF THE ANGULAR EMISSIVITY AND BLACK HOLE SPIN

The effect of applying a radial emissivity is straightforward. The transfer function describing all the relativistic effects from a given radial ring of the disc is unaffected, so the effect is simply to change the weighting of the line profile from each radial ring of the disc.

By contrast, the effect of the angular distribution is far more subtle. A given radial ring on the disc can contribute to the line profile from a range of emission angles. The relative

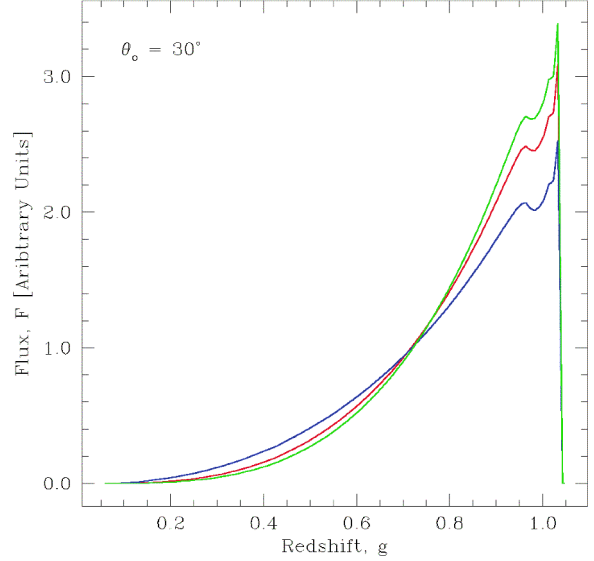


Figure 10. As in Fig. 9 with the disc now extending from $1.235 - 400r_g$. There is still a $\sim 25\%$ change in the blue wing height and significant change in red wing slope for the different angular emissivities, despite the inclusion of the outer disc regions.

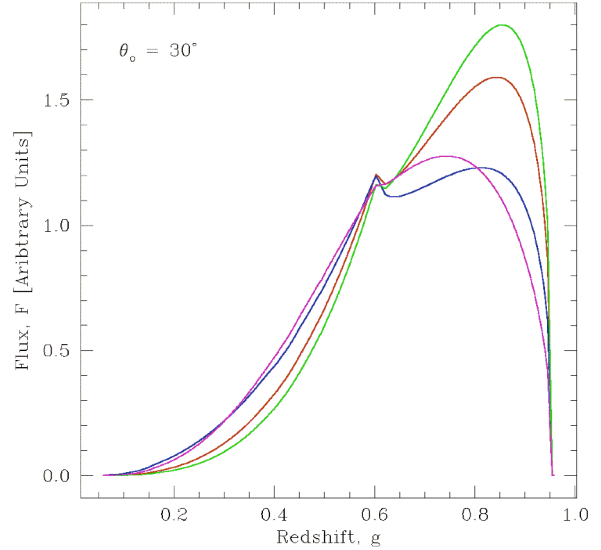


Figure 11. As in Fig. 9 with the disc now extending from $1.235 - 6r_g$. The additional magenta line is for a limb darkened angular emissivity with more centrally concentrated radial emissivity, $\propto r_e^{-4.5}$. This is very similar to the blue line profile derived from a very different radial emissivity, $\propto r_e^{-3}$, with a limb brightened angular emissivity.

weighting of these is determined by the angular emissivity, so it forms part of the calculation of the transfer function itself.

Different angular emissivity laws can have striking effects on the form of the relativistic line profile, which we illustrate in Fig. 9 for a maximal Kerr geometry ($a=0.998$) with the disc extending (as previously) from $1.235 - 20r_g$ and $\theta_o = 30^\circ$. The line profiles here all implement the stan-

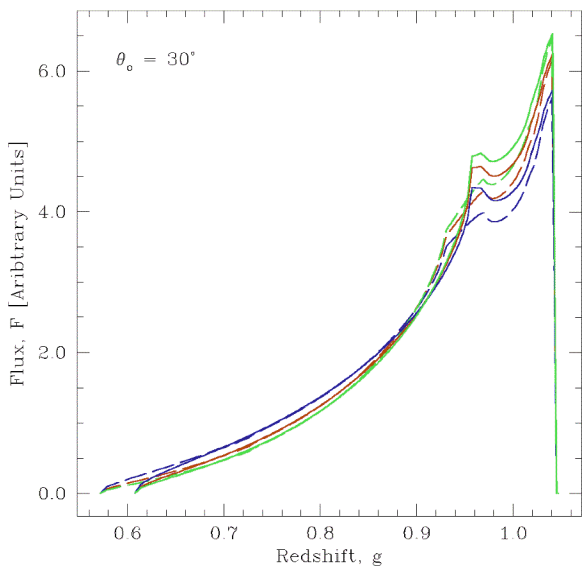


Figure 12. As in Fig. 9 but with the disc extending from $6-400r_g$ in an extreme Kerr (solid line) and Schwarzschild (dashed line) spacetime. The differences between the line profiles produced for the same sized disc in different assumed spacetimes is of order $\sim 5\%$ for a given angular emissivity. The effect of changing the angular emissivity is also similarly small ($\sim 5-10\%$). This contrasts with the much larger effects seen in the extreme Kerr metric for a disc extending down to $1.235r_g$, where lightbending is much more important (Fig. 9).

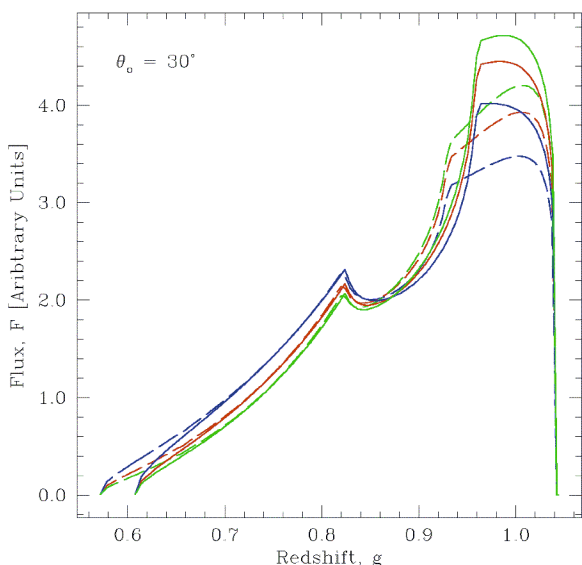


Figure 13. As in Fig. 12 but with the disc extending from $6-20r_g$. The differences now are of order 15-20%.

dard radial emissivity law of r^{-3} . However, we now compare a range of angular emissivity laws, these being (from top to bottom at the blue peak in Fig. 9) the standard limb darkening law (as discussed in §3.3), followed by the constant angular emissivity case (as used in §3.2). An ionized disc could also be limb *brightened*, with the probable limiting

case of $f(\mu) \propto 1/\mu$ as expected from optically thin material, shown as the bottom line in Fig. 9. There is a $\sim 35\%$ difference in the height of the blue peak depending of the form of the angular emissivity used.

However, such a limited range of radii is probably not very realistic. The disc should extend out to much greater distances from the black hole, where the relativistic effects (including lightbending) are less extreme. However, realistic emissivities strongly weight the contribution from the innermost regions, so the effective dilution of the relativistic effects by including the outer disc is not overwhelming. Fig. 10 shows the line profiles generated using the same angular emissivity laws for a disc extending from $1.235-400r_g$, again with $\theta_o = 30^\circ$. There are still significant differences in the line profiles, with a $\sim 25\%$ difference in the height of the blue peak while the red wing slope changes from $F_o(E_o) \propto E_o^{3.5}$ (limb darkened) to $\propto E_o^{2.5}$ (limb brightened).

Despite the expectation of an extended disc, some recent observational studies (e.g. Reynolds et al. 2004) have tentatively suggested that the disc is very small, from $\sim 1.235-6r_g$. This enhances the importance of lightbending. Fig. 11 shows the line profiles for a disc extending from $1.235-6r_g$ using the different angular emissivity laws of Fig. 9. The blue peak height differences are $\sim 40\%$, and the red wing slopes are different. For comparison we also show a limb darkened profile obtained from a very different *radial* emissivity of $r^{-4.5}$. This is very similar to the extreme limb brightened profile obtained from the r^{-3} radial weighting. We caution that uncertainties in the angular distribution of the line emissivity can change the expected line profile due to lightbending effects even at low/moderate inclinations, and that this can affect the derived radial emissivity.

Currently, the only available models in XSPEC have either zero or maximal spin. A zeroth order approximation to spacetimes with different spins is to use the maximal Kerr results but with a disc with inner radius given by the minimum stable orbit for the required value of a (e.g. Laor 1991). We test this for the most extreme case of $a = 0$ modelled by a maximal Kerr spacetime with $r_{min} = 6r_g$. Fig. 12 compares this with a true Schwarzschild calculation for a disc extending from $6-400r_g$ with $\theta_o = 30^\circ$ for a range of angular emissivities. The differences between the spacetimes (for a given angular emissivity) are at most $\sim 5\%$. This is roughly on the same order as the effect of changing the angular emissivity, which is much reduced here compared to Fig. 9 due to the larger r_{min} . Assumptions about both spin and angular emissivity become somewhat more important for smaller outer disc radii. Fig. 13 shows this for a disc between $6-20r_g$ (directly comparable to Fig. 7).

5 CONCLUSIONS

Recent observational studies have provided evidence for highly broadened fluorescent iron K α lines. While there are a variety of line profiles seen (e.g. Lubinski & Zdziarski 2001), there are some objects where the line implies that there is material down to the last stable orbit in a maximally spinning Kerr spacetime (most notably MCG-6-30-15: Wilms et al. 2001). However, the strong gravity codes generally used to model these effects are now over a decade old. Increased computer power means that it is now possible to

improve on these models. We describe our new code to calculate these effects, which uses fully adaptive gridding to map the image of the disc at the observer using the analytic solutions of the light travel paths. This is a very general approach, so the code can easily be modified to incorporate different emission geometries.

We compare the results of our new code with those from `diskline` and `laor` (publically available in the XSPEC spectral fitting package) for Schwarzschild and extreme Kerr spacetimes. These previous models are accurate to $\sim 10\%$ with realistic ($\propto r^{-3}$) radial emissivities. However, they make specific assumptions regarding the angular dependence of the emitted flux, which may or may not be valid. Light-bending is *always* important for a disc which extends down below $20r_g$, in that the image of the disc at the observer *always* consists of a range of different emission angles. This can produce significant changes to the derived line profile, especially in extreme Kerr spacetimes. Whilst calculating strong gravitational effects is a difficult numerical problem, the underlying physics is well known. By contrast, the *angular* emissivity is an astrophysical problem, and is not at all well known as it depends on the ionization state of the disc as a function both of height and radius. Before we can use the line profiles to provide a sensitive test General Relativity and probe the underlying physics, we will need to have a much better understanding of the astrophysics of accretion.

This code will be publically released for inclusion as a convolution model in the XSPEC spectral fitting package. This will include arbitrary spin and inner and outer disc radii as well as allowing both angular and radial emissivities to be specified.

After this paper was submitted we learnt of the independent work by (Dovciak, Karas & Yaqoob 2004) which also develops a new strong gravity code. Their results match very closely with those presented here.

ACKNOWLEDGEMENTS

We are grateful to an anonymous referee for useful comments and suggestions on previous versions of this manuscript. We would also like to thank E. Agol and M. Calvani for useful discussions and encouragement.

REFERENCES

- Agol E.; Ph.D. thesis, 1997, Univ. California, Santa Barbara.
- Ballantyne, D.R.; Ross, R.R.; Fabian, A.C. MNRAS 201, 327, 10.
- Blaes, O.M.; Physics Fundamentals of Luminous Accretion Disks Around Black Holes in "Accretion Disks, Jets, and High Energy Phenomena in Astrophysics", Proceedings of Session LXXVIII of Les Houches Summer School, Chamonix, France, August 2002.
- Cadez, A.; Fanton, C.; Calvani, M.; NEWA Vol. 3, No. 8, 647.
- Cadez, A.; Calvani, M.; Fanton, C.; MmSAI Vol. 74, 2003.
- Carter, B.; PhRv, 1968, 174.1559C.
- Chandrasekhar, S.; The Mathematical Theory of Black Holes, Oxford University Press, N.Y., 1983.
- Cunningham, C.T.; ApJ, 1975, 202, 788
- Cunningham, C.T.; Bardeen, J. M.; ApJ, 1973, 183, 237
- de Felice, F.; Preti, G.; Class. Quantum Grav. 1999, 16, 2929
- Dovciak, M.; Karas, V.; Yaqoob, T.; ApJ SS 2004, accepted (astro-ph/0403541).
- Ebisawa, K.; Mitsuda, K.; Hanawa, T.; ApJ, 1991, 367, 213
- Ebisawa, K.; Makino, F.; Mitsuda, K.; Belloni, T.; Cowley, A. P.; Schmidtke, P.C.; Treves, A.; ApJ, 1993, 403, 684
- Fabian, A.C.; Rees, M.J.; Stellar, L.; White, N. E.; MNRAS 1989, 238, 729.
- Falcke, H.; Melia, F.; Agol, E.; ApJ, 2000, 528, L13
- Fanton, C.; Calvani, M.; de Felice, F.; Cadez, A.; PASJ 1997, 49, 159
- Gierlinski, M.; Maciolek-Niedzwiecki, A.; Ebisawa, K.; MNRAS 2001, 325, 1253.
- Hollywood, J.M.; Melia, F.; ApJ 1997, 112, 423.
- Iwasawa, K.; Fabian, A.C.; Reynolds, C. S.; Nandra, K.; Otani, C.; Inoue, H.; Hayashida, K.; Brandt, W.N.; Dotani, T.; Kunieda, H.; Matsuoka, M.; Tanaka, Y.; MNRAS 1996, 282, 1038.
- Karas, V.; Martocchia, A.; Subr, L.; PASJ 2001, 53, 189
- Karas, V.; Vokrouhlicky, D.; Polnarev, A. G.; MNRAS 1992, 259, 569
- Kaspi, S. et al.; ApJ 2002, 574, 643
- Laor, A.; ApJ 1991, 376, 90.
- Laor, A.; Netzer, H.; MNRAS 1989, 238, 897.
- Laor, A.; Netzer, H.; Piran, T.; MNRAS 1990, 242, 560.
- Lubinski, P.; Zdziarski, A. A.; MNRAS 2001, 323, 37.
- Luminet, J-P.; A&A 1979, 75, 228.
- Makishima, K.; Kubota, A.; Mizuno, T.; Ohnishi, T.; Tashiro, M.; Aruga, Y.; Asai, K.; Dotani, T.; Mitsuda, K.; Ueda, Y.; Uno, S.; Yamaoka, K.; Ebisawa, K.; Kohmura, Y.; Okada, K.; ApJ 2000, 535, 632.
- Martocchia, A.; PhD Thesis, 2000, SISSA-ISAS, Trieste
- Martocchia, A.; Karas, V.; Matt, G.; MNRAS, 2000, 312, 817.
- Matt, G.; Perola, G.C.; Stella, L.; A&A, 1993, 267, 2, 643.
- Misner, C. S.; Thorne, K. S.; Wheeler, J. A.; Gravitation, W H Freeman, 1973.
- Nayakshin, S.; Kazanas, D.; Kallman, T. R. ApJ 2000, 537, 833.
- Rauch, K. P.; Blandford, R.D.; ApJ, 1994, 421, 46.
- Reynolds C.S.; Begelman, M.C.; ApJ, 1997, 488, 109.
- Reynolds C.S.; Wilms, J.; Begelman, M.C.; Staubert R., Kendziorra E.; MNRAS 2004 in press (astro-ph/0401305)
- Ross, R.R.; Fabian, A.C.; Young, A.J.; MNRAS 1999, 306, 461.
- Tanaka, Y.; Nandra, K.; Fabian, A.C.; Inoue, H.; Otani, C.; Dotani, T.; Hayashida, K.; Iwasawa, K.; Kii, T.; Kunieda, H.; Makino, F.; Matsuoka, M. Nature, 1995, 375, 659.
- Fabian, A. C. Vaughan, S. MNRAS 2003, 340, L28
- Viergutz, S. U.; A&A, 1993, 272, 355.
- Wilms, J.; Reynolds, C. S.; Begelman, M. C.; Reeves, J.; Molendi, S.; Staubert, R.; Kendziorra, E.; MNRAS 2001, 328, L27.
- Zakharov, A. F., Repin, S. V. A&A, 2003, 406, 7.
- Zycki, P. T.; Done, C.; Smith, D. A.; MNRAS 1998, 301, 231.